Monthly Notices of the ROYAL ASTRONOMICAL SOCIETY

MNRAS **504,** 5754–5767 (2021) doi:10.1093/mnras/stab1151
Advance Access publication 2021 April 23

Detection of complex organic molecules in young starless core L1521E

Samantha Scibelli [1]★ Yancy Shirley,[1] Anton Vasyunin[2] and Ralf Launhardt[3]

[1]*Steward Observatory, University of Arizona, Tucson, AZ 85721, USA*
[2]*Institute of Natural Sciences and Mathematics, Ural Federal University, 19 Mira Str, 620075 Ekaterinburg, Russia*
[3]*Max-Planck-Institut für Astronomie, Königstuhl 17, D-9117 Heidelberg, Germany*

Accepted 2021 April 15. Received 2021 March 19; in original form 2020 September 22

ABSTRACT

Determining the level of chemical complexity within dense starless and gravitationally bound pre-stellar cores is crucial for constructing chemical models, which subsequently constrain the initial chemical conditions of star formation. We have searched for complex organic molecules (COMs) in the young starless core L1521E, and report the first clear detection of dimethyl ether (CH_3OCH_3), methyl formate ($HCOOCH_3$), and vinyl cyanide (CH_2CHCN). Eight transitions of acetaldehyde (CH_3CHO) were also detected, five of which (A states) were used to determine an excitation temperature to then calculate column densities for the other oxygen-bearing COMs. If source size was not taken into account (i.e. if filling fraction was assumed to be one), column density was underestimated, and thus we stress the need for higher resolution mapping data. We calculated L1521E COM abundances and compared them to other stages of low-mass star formation, also finding similarities to other starless/pre-stellar cores, suggesting related chemical evolution. The scenario that assumes formation of COMs in gas-phase reactions between precursors formed on grains and then ejected to the cold gas via reactive desorption was tested and was unable to reproduce observed COM abundances, with the exception of CH_3CHO. These results suggest that COMs observed in cold gas are formed not by gas-phase reactions alone, but also through surface reactions on interstellar grains. Our observations present a new, unique challenge for existing theoretical astrochemical models.

Key words: astrochemistry – radiative transfer – submillimetre: ISM.

1 INTRODUCTION

The chemistry of star and planet formation begins with the synthesis of molecules in interstellar molecular clouds. Dense ($\sim 10^5$ cm^{-3}) and cold (10 K) regions within these clouds, called starless and gravitationally bound pre-stellar cores, represent the earliest observable stage of low-mass (M $\leq$ few M$_\odot$) star-formation (di Francesco et al. 2007; Bergin & Tafalla 2007; André et al. 2014). It is during this phase, prior to the formation of a first hydrostatic core (the foremost stage of a protostar), that the initial conditions for star and planet formation are set.

In the warm regions of early star formation, such as in hot cores and hot corinos, rich chemistry has been explained by a warm-up, gas-phase chemistry driven by the heat from the forming protostar that sublimates ice mantles (Jørgensen, Belloche & Garrod 2020 and references therein). Surprisingly, even in cold and shielded environments, rotational transitions of complex organic molecules (COMs) have been detected in the gas phase towards dense pre-stellar cores from deep millimeter wave observations (Öberg et al. 2010; Bacmann et al. 2012; Jiménez-Serra et al. 2016; Scibelli & Shirley 2020). These large ($\geq$6 atom) carbon-bearing molecules are of astrobiological significance; and their presence prior to protostar and planet formation provides insight into COM formation histories.

There is still, however, a significant gap in our understanding of the development of COMs during this initial phase of low-mass star formation. The traditional picture depicts COMs forming in CO and H_2O rich ices that are irradiated by UV light and cosmic rays (Watanabe & Kouchi 2002; Chuang et al. 2017). The subsequent formation of radicals in the warming ice, during the development of a hot corino, leads to the formation of complex organic species that are released into the gas phase when the young, accreting protostar heats up the dust grains above the sublimation temperature of the ices (Garrod & Herbst 2006; Aikawa et al. 2008; Herbst & van Dishoeck 2009). Since pre-stellar cores have no internal heating source, several different scenarios of cold COMs formation have been proposed, including the desorption of radicals, yet their relative importance is not currently clear.

If COMs form in the ices, then the subsequent desorption of COMs in the outer, icy layers of pre-stellar cores appears to occur at a rate fast enough to build up an observable abundance of COMs (Vastel et al. 2014). Alternatively, COMs could form in the gas phase through neutral–neutral reactions from the chemical desportion of radicals formed in the ice (Vasyunin & Herbst 2013; Vasyunin et al. 2017). New non-diffusive chemical models produce excited radicals instead by surface or bulk reactions, which leads to an enhancement of COM abundance in cold core conditions (Jin & Garrod 2020). In order to discern between different formation scenarios, we must understand the physical conditions in which COMs form as well as constrain their abundances.

The discovery of COMs in pre-stellar cores leads to fundamental questions of how quickly these COMs form, and to what level of

★ E-mail: sscibelli@email.arizona.edu

complexity. In our previous study of a large sample (31) of starless and pre-stellar cores within the Taurus Molecular Cloud (Scibelli & Shirley 2020), we found a prevalence of the 'mother molecule,' methanol (CH_3OH; 100 per cent detection rate), which is the gas precursor of several COMs, as well as acetaldehyde (CH_3CHO; 70 per cent detection rate). For the larger molecules, like dimethyl ether (CH_3OCH_3) and methyl formate ($HCOOCH_3$), surveys have been limited to a few well-studied, evolved, and dense objects, i.e. L1689B in Ophiuchus (Bacmann et al. 2012) and L1544 in Taurus (Jiménez-Serra et al. 2016). L1544 is the densest known pre-stellar core, with well developed collapse motions and a central density $>10^7$ cm^{-3} (Caselli et al. 2019). Species such as CH_3O, CH_3CHO, and CH_3OCH_3 are enhanced in L1544 by factors of $\sim$2−10 towards the CH_3OH peak with respect to (w.r.t.) the core's centre (Jiménez-Serra et al. 2016). It has been suggested that $HCOOCH_3$ and CH_3OCH_3 are synthesized in gas-phase reactions with CH_3OH and other precursor species ejected from grains via the process of reactive desorption (Vasyunin et al. 2017). We know that CH_3OH and CH_3CHO are prevalent in the starless and pre-stellar cores in Taurus (Scibelli & Shirley 2020), now we look for more complex species.

In this study, we targeted a dynamically and chemically young starless core in Taurus, Lynds 1521E (L1521E). It has a modest central density of $2-3 \times 10^5$ cm^{-3}, no kinematic evidence for collapse, little evidence for freezout of CO (factor of $\lesssim$2), and little evidence for chemically evolved indicators, such as abundant deuterated molecules (Tafalla & Santiago 2004; Ford & Shirley 2011). L1521E can only have existed at its present density of $>10^5$ cm^{-3} for less than 10^5 yr, otherwise there would be more significant CO freezout (e.g. see Redman et al. 2002). Uniquely, L1521E is also one of only two cores known in Taurus, the other Seo 32 in the B213 region, where the 'early-time' chemical tracers (such as CCS and HC_5N) peak strongly at the same position as the dust continuum peak (Suzuki et al. 1992; Seo et al. 2019). Furthermore, 'late-time' chemical tracers such as NH_3, N_2H^+, and deuterated species are very weak (Hirota, Ikeda & Yamamoto 2001; Nagy et al. 2019). The chemical and kinematical evidence agree that this object is one of the youngest starless cores known, with densities at $>10^5$ cm^{-3}. Thus, L1521E is an excellent object towards which to test the limits of how quickly COMs form, to test what level of chemical complexity COMs form, and to test at what molecular abundances COMs form.

We present detections and detailed column density analyses for multiple COMs towards the young starless core L1521E. In Section 2, we discuss the line observations made by the Arizona Radio Observatory (ARO) 12-m telescope. In Section 3, we discuss our process for estimating the H_2 column density as well as the line analysis for each molecule detected. Included is a detailed description of non-detected transitions as well as discussion of glycoaldehyde (cis-CH_2OHCHO), which was targeted but not detected and known as an important molecule for building up sugars of astrobiological importance (see Jiménez-Serra et al. 2020). We also calculate column densities and account for the beam filling factor. We then discuss how our results compare to other sites of low-mass star formation, as well as to modelled abundances, in Section 4. Lastly, we summarize our results in Section 5.

2 ARO 12-M OBSERVATIONS

Molecular line observations were made with the ARO 12-m telescope during three separate seasons, 2 yr apart, using two different backend receivers. The first observing shifts between 2017, January 12 and April 27 with 10 tunings between 84 and 102 GHz (3.6–2.9 mm). The sideband separating, dual polarization 3-mm ALMA prototype receiver was used with the MAC backend in a mode with 300-MHz bandwidth with 48.8-kHz resolution (bandwidth of 880–1060 km s^{-1} with 0.14–0.17 km s^{-1} resolution). Two IFs within the same sideband were connected to the Vertical (Vpol) and Horizontal (Hpol) polarization feeds. The lower sideband was used for frequencies less than 97 GHz while the upper sideband was used for frequencies higher than 97 GHz. The rejection between sidebands was measured by injecting a tone into the opposite sideband and measuring the strength of the signal in the observed sideband. The sideband rejection was $\geq$18 dB for all tunings.

The second set of observing shifts took place between 2019 May 12th and June 25th with three different tunings on the 3-mm receiver between 84 and 99 GHz (3.6–3.0 mm), and four tunings on the 4-mm receiver between 69 and 77 GHz (3.8–4.3 mm). These observations used the new AROWS backend in a mode with 125-MHz bandwidth and 19.5-kHz resolution. There was a third set of observations that took place between 2019, February 17th and 27th utilizing the AROWS backend, tuned to the 79-GHz $HCOOCH_3$ transitions with the 4-mm receiver.

Position-switched observations of L1521E were centred on the 850-μm dust continuum peak position of $4^h\,29^m\,14\overset{s}{.}9 + 26^\circ\,13'\,56\overset{''}{.}6$ J2000.0, with 5–6 min total integration time (ON+OFF) between calibration scans (longer in good weather). During the first observing run, measurements of Venus and Mars were used to determine the average beam efficiency. Values were consistent for all 3-mm tunings with an average value of $\eta_{\rm mb,MAC,3\,mm} = 0.87 \pm 0.01$. Additionally, a factor of 1.14 needed to be multiplied to the final main beam temperature due to systematic calibration error present in the software of the MAC. The MAC antenna temperature was found to be 14 per cent lower than the new more trusted AROWS backend (see Scibelli & Shirley 2020). For the two remaining observing runs, AROWS was used and average beam efficiencies for the 3- and 4-mm observations were calculated separately. We note that during the Summer between the first observing run (MAC) and the second and third sessions (AROWS), the antenna surface accuracy was improved. During the second run, we used observations of just Mars to get an average value of $\eta_{\rm mb,AROWS,3\,mm} = 0.91 \pm 0.01$ for all 3-mm tunings. For the 4-mm tunings, we average Venus, Mars, and Jupiter measurements to determine an average beam efficiency of $\eta_{\rm mb,AROWS,3\,mm} = 0.93 \pm 0.01$. In the third observing session, exclusively set to a 4-mm tuning, the average beam efficiency was calculated to be $\eta_{\rm mb,AROWS,4\,mm} = 0.92 \pm 0.01$, using Jupiter and Mars measurements.

Each tuning was chosen to include one or more COMs within the bandpass. Simple local thermal equilibrium (LTE), excitation analyses were performed to estimate the most likely line to be observed in the 3-mm(4-mm) bandpass. In LTE, the same excitation temperature is assumed for all transitions, which we have to assume is true because no collisional rates are available. In Scibelli & Shirley (2020), excellent agreement was found when both the LTE and non-LTE methods were applied to methanol, CH_3OH, which does have published collisional rates. Data reduction was performed using the CLASS programme of the GILDAS package.[1] The AROWS spectra have been hanning smoothed by two channels since the default software writes out the data at half the actual resolution.

[1] http://iram.fr/IRAMFR/GILDAS/

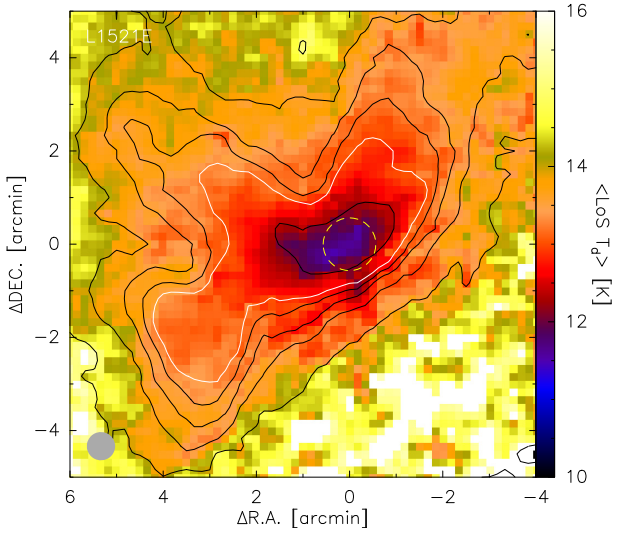

Figure 1. A map of the average line-of-sight dust temperature (colour scale) and column density (contours) determined from SED fitting of *Herschel Space Observatory* observations at 250, 350, and 500 μm centred on L1521E at $4^{h}\,29^{m}\,14\overset{s}{.}9 + 26^{\circ}\,13'\,56\overset{''}{.}6$ J2000.0. The N_H contours correspond to 2, 4, 6, 8, 10, 20 $\times$ 10^{21} cm^{-2} (for N_{H_2}, divide by 2). The yellow dashed circle indicates the average 12-m beam size within which we find an average $\langle N_{H_2} \rangle = 1.6 \times 10^{22}$ cm^{-2}.

3 ANALYSIS AND RESULTS

3.1 Dust continuum

Launhardt et al. (2013) developed a continuum pixel-by-pixel SED fitting technique to model the average line-of-sight dust temperature distribution and the H_2 column density (assuming a total gas mass to dust mass ratio of 150:1 and OH5 dust opacities; Ossenkopf & Henning 1994) from *Herschel Space Observatory* and other FIR and submillimeter observations. L1521E was observed with MIPS on the *Spitzer Space Telescope* at 160 μm and with SPIRE on the *Herschel Space Observatory* at 250, 350, and 500 μm. Unfortunately, no PACS observations of L1521E exist. MIPS observations have severe instrumental artifacts that prohibit detailed, pixel-by-pixel modelling of that image but a total flux may be used as a constraint when modelling the integrated SED (Kirk, Johnstone & Tafalla 2007). L1521E was also observed with SCUBA at the 15-m JCMT (Kirk, Ward-Thompson & André 2005), but this map was too small to recover the emission level from the extended envelope and could therefore not easily be combined with the *Herschel* data. The data reduction, including colour corrections, of the *Herschel*/SPIRE data is described in Launhardt et al. (2013). The results of SED modelling the archival *Herschel* data are shown in Fig. 1.

The central regions of L1521E have peak column densities of $N_H = 3.9 \times 10^{22}$ cm^{-2} and average line-of-sight dust temperatures of 11 K. The average H_2 density within the typical 12-m beam size of 1 arcmin (corresponding to $\sim$8400 au at 140 pc) is $N_{H_2} = 1.6 \times 10^{22}$ cm^{-2}. We used this average H_2 column density for all subsequent calculations of molecular abundances. The corresponding mass is 2.2 $M_\odot$. Our SPIRE image modelling results are consistent within a factor of 2 in column density with the analysis of SPIRE-FTS observations by Makiwa et al. (2016).

Using the 850-μm JCMT map and the same techniques and grid of radiative transfer models described in Shirley et al. (2005), we find that a thermally supported Bonnor–Ebert sphere with a central density of 3×10^5 cm^{-3} is the best-fitted model. This result is consistent with our archival *Herschel* SED modelling and the published radiative transfer modelling of MAMBO 1.2-mm data from Tafalla & Santiago (2004) ($n(r) = 2.7 \times 10^5$ cm^{-3}/[1 + (r/6.3 $\times$ 10^{16} cm)^2]). We use these density profiles to calculate the virial parameter, $\alpha_{vir} = 3R\sigma_v^2/a_1 GM(R)$. The line-of-sight velocity dispersion, $\sigma_v = 0.25 \pm 0.02$ km s^{-1}, is calculated from the average and standard deviation of the observed linewidths towards the dust continuum peak in Nagy et al. (2019) and is corrected for the molecule specific thermal broadening and the sound speed (Fuller & Myers 1992). The density profile correction factor, a_1, is calculated using the techniques described in the appendices of Bertoldi & McKee (1992) and Sipilä, Harju & Juvela (2011). The exact radius of L1521E is uncertain and depends on how the core boundary is defined (i.e. for examples of various definitions see Benson & Myers 1989; Pattle et al. 2015; Seo et al. 2015; Chen et al. 2019). Assuming that it is in between angular radii of 60–140 arcsec, then we find that α_{vir} is between 1.8 and 0.9 which would indicate that L1521E is near the typical dividing line between a starless core and a gravitationally bound pre-stellar core. We shall continue to use the more general term starless when referring to the L1521E core.

3.2 Molecular identifications

With confidence, we report the first detection of CH_3OCH_3, $HCOOCH_3$, and CH_2CHCN in the young starless core L1521E. Additionally, eight transitions of CH_3CHO and seven transitions of CH_2CHCN were detected, each set used to construct rotation diagrams to constrain excitation temperature and column density. The properties of the observed lines are listed in Table 1. For each transition, we calculated the integrated intensity over the line and its uncertainty from the following equation

$$I \pm \sigma_I = \sum_i T_i \delta v_{\rm ch} \pm \sigma_T \sqrt{\frac{3\Delta v_{\rm FWHM} \delta v_{\rm ch}}{\sqrt{2 \ln 2}}}, \quad (1)$$

where $\delta v_{\rm ch}$ is the spectrometer velocity resolution; and σ_T is the baseline rms. The integrated intensity and uncertainty are calculated over a velocity range corresponding to the $\pm 3\sigma$ width of a Gaussian with the same integrated intensity. This technique works well for lines that are Gaussian and do not have significant skewness (for instance due to outflows), which is the case for all lines observed towards L1521E. The median FWHM for our lines is at 0.35 km s^{-1} (see Table 2). We note that in Table 2 there is slight discrepancy in $v_{\rm LSR}$ for the two transitions of CH_2CHCN which were detected with the old (less trustworthy) MAC backend receiver. Otherwise, the $v_{\rm LSR}$ of the remaining lines lie at $\sim$7 km s^{-1} (median value of 6.97 km s^{-1}). In the following subsections, we present an overview of the molecules detected.

3.2.1 *Acetaldehyde (CH_3CHO)*

A total of eight transitions of CH_3CHO were detected by tuning to 3- and 4-mm rotational transitions suitable for 10 K gas, i.e. those with values for $E_u/k < 15$ K (spectroscopic work detailed in Kleiner, Lovas & Godefroid 1996). Observed spectra are plotted in Fig. 2. With both the MAC and the AROWS backends, we observed the 96 GHz $5_{0,5} - 4_{0,4}$ A and E transitions, however, we only report on the AROWS detection here. The weak CH_3CHO $3_{1,3} - 2_{0,2}$ A transition at 101.89 GHz was detected with only the MAC. The remaining transitions were detected exclusively with the AROWS backend, at $\sim$0.07–0.08 km s^{-1} resolution. The weakest transition,

Table 1. Complex organic molecule fit results.

Molecule	Transition	ν (GHz)	E_u/k (K)	$^a g_u$	A_{ul} (s^{-1})	T_{mb} (mK)	$\sigma(T_{mb})$ (mK)	$I(T_{mb})$ (mK km s^{-1})	$\sigma(I)$ (mK km s^{-1})
CH_3CHO	$3_{1,3} - 2_{0,2}$ A[a]	101.89241	7.7	14	4.0E-06	23.0	4.0	10.7	1.3
	$5_{0,5} - 4_{0,4}$ A	95.96347	13.8	22	3.0E-05	89.0	9.0	30.0	2.0
	$5_{0,5} - 4_{0,4}$ E	95.94744	13.9	22	3.0E-05	51.0	8.0	23.0	2.0
	$2_{1,2} - 1_{0,1}$ A	84.21975	5.0	10	2.4E-06	23.0	4.0	7.1	0.8
	$4_{0,4} - 3_{0,3}$ A	76.87895	9.2	18	1.5E-05	89.0	11.0	36.0	3.0
	$4_{0,4} - 3_{0,3}$ E	76.86644	9.3	18	1.5E-05	103.0	10.0	41.0	3.0
	$4_{1,4} - 3_{1,3}$ A	74.89168	11.3	18	1.3E-05	53.0	11.0	14.0	2.0
	$4_{1,4} - 3_{1,3}$ E	74.92413	11.3	18	1.3E-05	48.0	9.0	13.0	2.0
CH_3OCH_3	$4_{1,4} - 3_{0,3}$ AA	99.32607	10.2	90	5.5E-06	9.1	3.0	2.9	0.6
	$4_{1,4} - 3_{0,3}$ EE	99.32522	10.2	144	5.5E-06	10.0	3.0	4.2	0.7
	$4_{1,4} - 3_{0,3}$ AE+EA	99.32436	10.2	90	5.5E-06	4.6	3.0	5.5	1.2
	$4_{2,3} - 4_{1,4}$ EE [a]	93.85710	14.7	144	3.6E-06	–	2.0	–	0.8
	$2_{2,1} - 2_{1,2}$ EE [a]	89.69981	8.4	80	2.3E-06	–	2.0	–	0.8
$HCOOCH_3$	$8_{1,8} - 7_{1,7}$ A [a]	89.31664	20.1	34	1.0E-05	–	4.0	–	1.3
	$8_{1,8} - 7_{1,7}$ E [a]	89.31466	20.2	34	1.0E-05	–	4.0	–	1.3
	$7_{0,7} - 6_{0,6}$ A	79.78389	15.7	30	7.2E-06	11.0	3.0	6.4	0.6
	$7_{0,7} - 6_{0,6}$ E	79.78171	15.7	30	7.2E-06	12.0	3.0	3.9	0.9
CH_2CHCN	$11_{0,11} - 10_{0,10}$	103.57539	29.9	69	8.8E-05	–	3.0	–	0.6
	$10_{1,9} - 9_{1,8}$	96.98245	27.8	63	7.2E-05	14.0	3.0	4.8	0.6
	$10_{0,10} - 9_{0,9}$	94.27664	24.9	63	6.2E-05	27.0	4.0	8.0	0.9
	$10_{1,10} - 9_{1,9}$	92.42626	26.6	63	6.8E-05	18.0	3.0	4.4	0.6
	$5_{1,5} - 4_{0,4}$ [a]	89.13091	8.8	33	1.8E-06	–	2.0	–	0.8
	$9_{1,8} - 8_{1,7}$ [a]	87.31281	23.1	57	5.3E-05	24.0	5.0	9.9	1.9
	$9_{0,9} - 8_{0,8}$ [a]	84.94600	20.4	57	4.9E-05	30.0	4.0	12.0	1.7
	$8_{1,7} - 7_{1,6}$	77.63384	18.9	51	3.6E-05	37.0	5.0	12.5	1.3
	$8_{0,8} - 7_{0,7}$	75.58569	16.3	51	3.4E-05	50.0	5.0	16.9	1.3
cis-CH_2OHCHO	$5_{2,4} - 4_{1,3}$[a]	87.76453	10.7	11	8.6E-06	–	4.0	–	1.4
	$8_{1,8} - 7_{0,7}$ [a]	85.78224	18.9	17	1.5E-05	–	3.0	–	1.2
	$8_{0,8} - 7_{1,7}$ [a]	82.47067	18.8	17	1.3E-05	–	4.0	–	1.3

Notes. [a]Transitions targeted with the MAC backend. Values for CH_3CHO and $HCOOCH_3$ from JPL catalog (https://spec.jpl.nasa.gov/; Pickett et al. 1998) and for the remaining transitions from CDMS data base (https://cdms.astro.uni-koeln.de; Müller et al. 2001, 2005; Endres et al. 2016). We note that A_{ul} can be calculated by the following equation, $A_{ul} = (64\pi^4\nu_i^3/3hc^3)\,(S\mu^2/(2J'+1))$, where J′ is the upper J in the transition and line strength, S, can be interpolated from values tabulated in Standards & Wacker (1969).

Table 2. Line FWHM and v_{LSR}.

Molecule	Transition	ν (GHz)	FHWM (km s^{-1})	v_{LSR} (km s^{-1})
CH_3CHO	$3_{1,3} - 2_{0,2}$ A[a]	101.89241	0.44[0.07]	6.96[0.03]
	$5_{0,5} - 4_{0,4}$ A	95.96347	0.42[0.05]	7.10[0.02]
	$5_{0,5} - 4_{0,4}$ E	95.94744	0.50[0.08]	7.08[0.03]
	$2_{1,2} - 1_{0,1}$ A	84.21975	0.29[0.07]	7.10[0.02]
	$4_{0,4} - 3_{0,3}$ A	76.87895	0.38[0.05]	7.18[0.02]
	$4_{0,4} - 3_{0,3}$ E	76.86644	0.37[0.04]	7.12[0.02]
	$4_{1,4} - 3_{1,3}$ A	74.89168	0.24[0.11]	7.16[0.03]
	$4_{1,4} - 3_{1,3}$ E	74.92413	0.27[0.10]	7.12[0.03]
CH_3OCH_3	$4_{1,4} - 3_{0,3}$ AA	99.32607	0.30[0.07]	6.97[0.03]
	$4_{1,4} - 3_{0,3}$ EE	99.32522	0.39[0.07]	7.13[0.04]
	$4_{1,4} - 3_{0,3}$ AE+EA	99.32436	1.14[0.34]	6.93[0.14]
$HCOOCH_3$	$7_{0,7} - 6_{0,6}$ A	79.78389	0.57[0.09]	6.96[0.05]
	$7_{0,7} - 6_{0,6}$ E	79.78171	0.32[0.08]	6.89[0.04]
CH_2CHCN	$10_{1,9} - 9_{1,8}$	96.98245	0.31[0.06]	6.85[0.03]
	$10_{0,10} - 9_{0,9}$	94.27664	0.27[0.06]	6.85[0.02]
	$10_{1,10} - 9_{1,9}$	92.42626	0.22[0.06]	6.86[0.02]
	$9_{1,8} - 8_{1,7}$ [a]	87.31281	0.38[0.07]	6.26[0.03]
	$9_{0,9} - 8_{0,8}$ [a]	84.94600	0.37[0.05]	6.55[0.02]
	$8_{1,7} - 7_{1,6}$	77.63384	0.31[0.05]	6.91[0.02]
	$8_{0,8} - 7_{0,7}$	75.58569	0.32[0.04]	7.02[0.02]

Note. [a]Transitions targeted with the MAC backend.

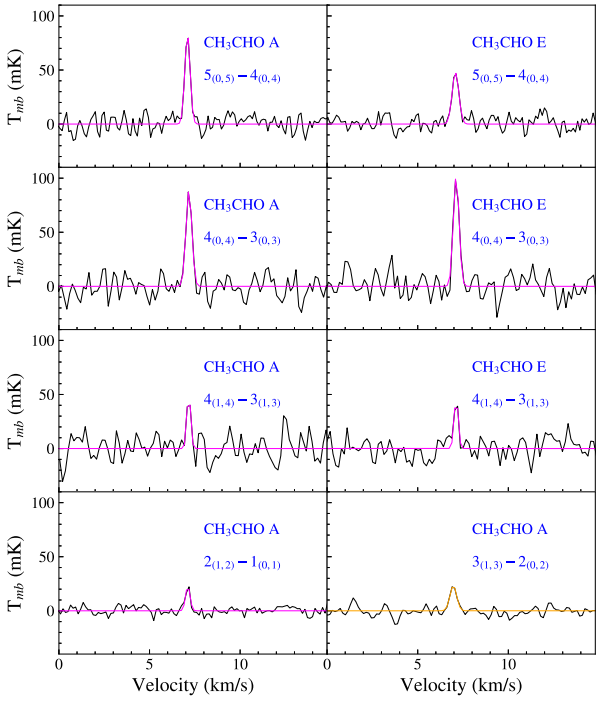

Figure 2. Spectra of all eight CH_3CHO transitions detected. In all panels except the bottom right-hand, the Gaussian fits are overplotted in magenta, for those detected with the AROWS backend receiver. In the bottom right-hand plot, the Gaussian fit is overplotted in orange and was observed with the MAC backend receiver. Each line peaks at the v_{LSR} ($\sim$7 km s^{-1}) of L1521E.

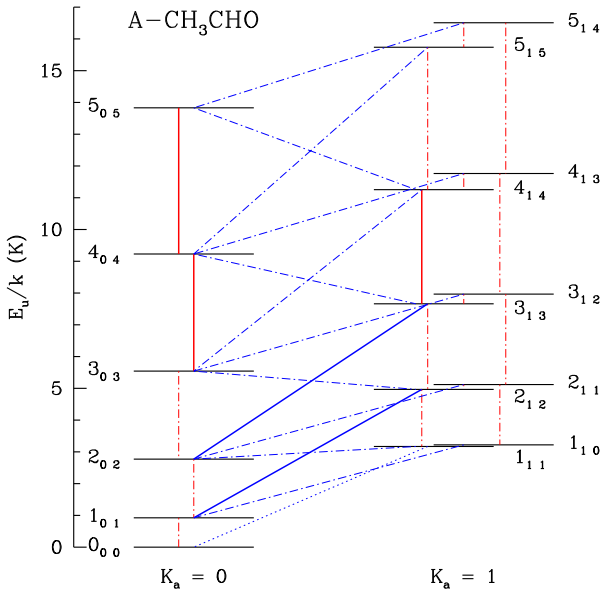

Figure 3. The rotational energy level diagram for CH_3CHO A. Solid red lines connect a-type ($\Delta K_a = 0$, $\Delta K_c = \pm 1$) transitions and solid blue lines connect b-type ($\Delta K_a = \pm 1$, $\Delta K_c = \pm 1$) transitions. Each solid line represents those transitions detected in L1521E. See fig. 2 in Gilmore et al. (1976 for a more complete energy level diagram.

CH_3CHO A $2_{1,2} - 1_{0,1}$ at 84 GHz, was targeted and detected with 4σ confidence. The remaining transitions, each various K levels of $J = 4-3$ (refer to Fig. 3), were targeted with the 4-mm receiver. The 76.9 GHz, $4_{0,4} - 3_{0,3}$ transitions are brightest. Each A and E

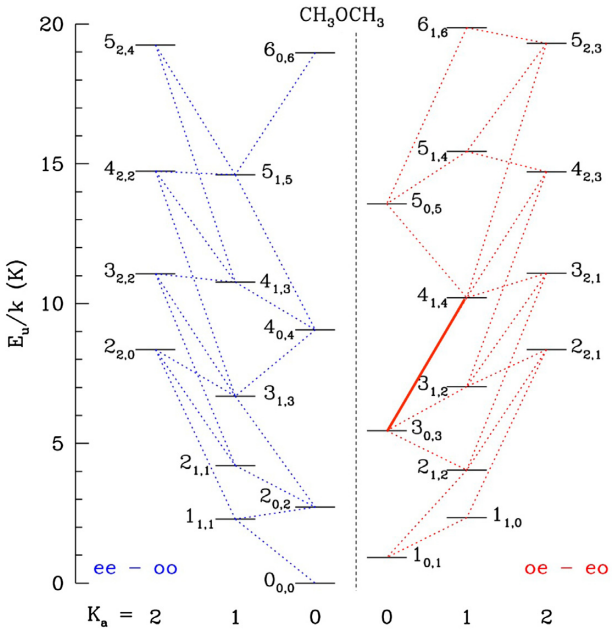

Figure 4. The rotational energy level diagram for CH_3OCH_3 EE with only the stronger b-type transitions shown ($\Delta K_a = \pm 1$, $\Delta K_c = \pm 1$). Weaker c-type transitions are not shown ($\Delta K_a = \pm 1$, $\Delta K_c = 0$). A solid red line connects the $4_{1,4}$ and $3_{0,3}$ levels, which produces the CH_3OCH_3 EE transition detected in L1521E.

pair were observed in the same bandpass. For the 95.95 GHz A and E states, they have a ratio of around 9:5, unlike the 76.9 and 74.9 GHz transitions with ratios close to the LTE statistical ratio of 1:1. Observations of A to E ratios of 1:1 have been observed towards other sources (Bacmann et al. 2012; Taquet et al. 2017).

3.2.2 *Dimethyl Ether (CH_3OCH_3)*

A simple LTE excitation analysis of CH_3OCH_3 shows that the $4_{1,4} - 3_{0,3}$ transition at 99.325 GHz should be the strongest line in the 3-mm band for gas at 10 K (spectroscopic work detailed in Neustock et al. 1990). Furthermore, the upper state energy level ($J_{K_a,K_c} = 4_{1,4}$) can only radiate (via electric dipole radiation) through this single transition (see Fig. 4). For CH_3OCH_3, there is an advantage of having torsional splitting of the rotational levels, as the lines manifest as three closely spaced lines ($\sim$2 MHz) with LTE statistical weights of 1:2:1 that are in a distinct, easy to identify pattern.

We observed CH_3OCH_3 during both observing sessions, further verifying its detection. A 93-h (total observing time), multishift integration with baseline rms of 1.9 mK using the MAC backend was successful in detecting the $4_{1,4} - 3_{0,3}$ transition (right-hand panel of Fig. 5), with three distinct peaks of signal-to-noise > 6 in integrated intensity at the correct frequencies for the AA, EE, and AE+EA species of CH_3OCH_3. During the second round of observations, we integrated for 166 h, down to an rms of 3.0 mK with the AROWS backend, confirming the previous MAC spectrometer detection (left-hand panel of Fig. 5). The EE species is the brightest line detected with $\sim 4\sigma$ confidence. By re-observing with AROWS, we gained higher spectral resolution, resolving linewidths. Values from the AROWS observation are reported in Table 1.

Attempts to detect the $4_{2,3} - 4_{1,4}$ and $2_{2,1} - 2_{1,2}$ transitions of CH_3OCH_3 during the first observing run were unsuccessful despite a baseline rms value of 2.2 mK for both lines. We calculate a 3σ upper limit to the integrated intensity of 0.8 mK km s^{-1}, assuming the same

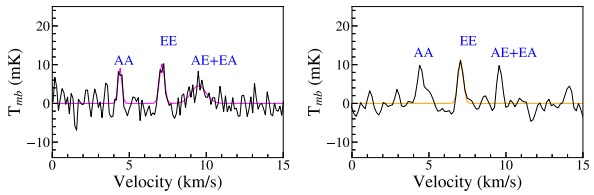

Figure 5. CH_3OCH_3 observations from first observing run with the MAC backend (right-hand panel) and the second observing run with the new AROWS backend (left-hand panel), at a higher velocity resolution. The centre EE transition peaks at the v_{LSR} of L1521E.

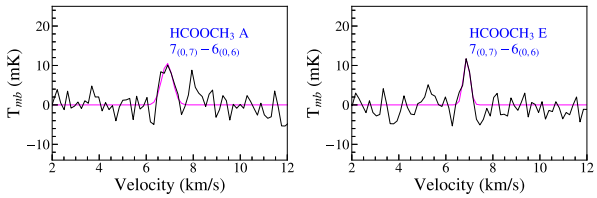

Figure 6. Two transitions of the 79 GHz $7_{0,7} - 6_{0,6}$ A and E states of $HCOOCH_3$ detected in L1521E, centred on the v_{lsr} of L1521E.

FWHM linewidth as observed for the $4_{1,4} - 3_{0,3}$ EE transition that was observed with the MAC backend, i.e. FWHM = 0.42 km s^{-1}. Each of the upper states of these transitions have multiple possible routes to radiate to lower energy levels. The transitions targeted in the 3-mm band do not have the largest branching ratio among those transitions, which mitigate their intensity (refer to Fig. 4).

3.2.3 Methyl Formate ($HCOOCH_3$)

Methyl formate, written as $HCOOCH_3$ or CH_3OCHO, was detected in the 4-mm band but not in the 3-mm band (spectroscopic work detailed in Ilyushin, Kryvda & Alekseev 2009). We find the 76-GHz transitions are more favourable for detection in cold L1521E, in part due to the lower upper energies (E_u/k = 15.7 K), when compared to the 89-GHz transitions (E_u/k = 20 K). We report detections of the 79 GHz $7_{0,7} - 6_{0,6}$ A and E transitions (observed in the same bandpass), reported with 3σ confidence (Fig. 6). The 89 GHz $8_{1,8} - 7_{1,7}$ A and E transitions of $HCOOCH_3$ have been detected before (see Taquet et al. 2017), yet we only report upper limits in Table 1 after getting down to rms of 3.5 mK.

3.2.4 Vinyl Cyanide (CH_2CHCN)

Seven transitions of vinyl cyanide (CH_2CHCN) were detected and plotted in Fig. 7 (spectroscopic work detailed in Costain & Stoicheff 1959). Another two transitions were not detected; and we report upper limits in Table 1. CH_2CHCN is the most COM we detect with a nitrogen atom. The strongest transition detected is the $8_{0,8} - 7_{0,7}$ a-type transition, with 8σ confidence. The $9_{0,9} - 8_{0,8}$ transition is the second strongest; and the $9_{1,8} - 8_{1,7}$ transition is slightly weaker.

Since the upper state of the two 9 − 8 transitions from MAC observations have similar energies (20.4 and 23.1 K respectively), they do not give a strong constraint on T_{ex}. The non-detection of the weaker $5_{1,5} - 4_{0,4}$ b-type transition with a much lower upper energy state (E_u/k = 8.8 K), does give a 3σ upper limit and constrains T_{ex} > 5 K. This is higher than the excitation temperatures that we derive for CH_3CHO, but perhaps not surprising since we detected even higher

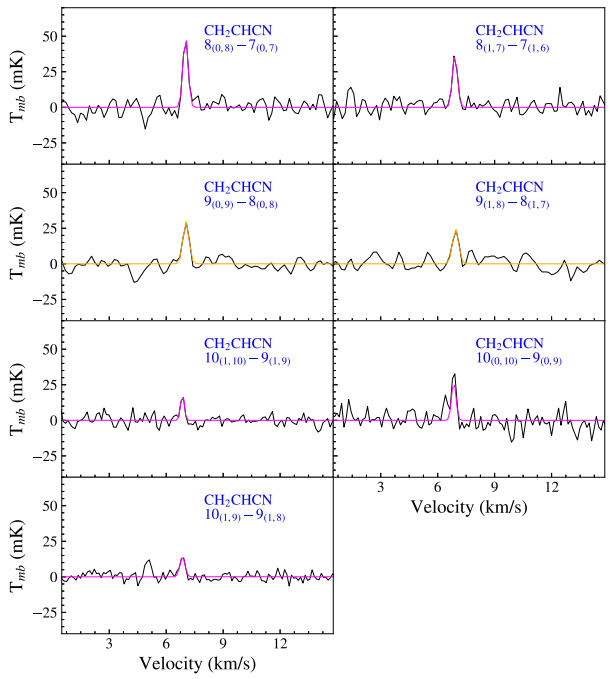

Figure 7. Spectra of seven separate transitions of CH_2CHCN. We note that the $J = 9 - 8$ transitions were detected earlier with the MAC and the Gaussian fit is displayed in orange. Each transition is centred on the v_{LSR} of L1521E.

energy transitions, up to $10_{1,9} - 9_{1,8}$ with an upper energy of E_u/k = 27.8 K.

We note that CH_2CHCN was recently detected and mapped in Titan's atmosphere with ALMA (Lai et al. 2017). Of astrobiological interest, CH_2CHCN is thought to be important as a potential molecule to form membranes in Titan's liquid methane oceans.

3.3 Molecular non-detections

Mock integrated intensity values for transitions of CH_3OCH_3, $HCOOCH_3$, and CH_2CHCN that were not detected were calculated based on the column density calculated from the detected transitions and assuming the same T_{tex} (and f_ν = 1). We also plot the LTE modelled Gaussian fits over the spectra in Fig. 8. For CH_3OCH_3, the 3σ upper limit to the integrated intensity is 2.4 mK km s^{-1}. The simulated integrated intensity for the $4_{2,3} - 4_{1,4}$ transition, assuming the same excitation temperature of 4.5 K, is below this limit at 1.1 mK km s^{-1}. Similarly, the simulated integrated intensity for the $2_{2,1} - 2_{1,2}$ transition was 1.7 mK km s^{-1}, below the 3σ upper limit. For both $8_{1,8} - 7_{1,7}$ transitions of $HCOOCH_3$, a 3σ upper limit to the integrated intensity is calculated to be 3.9 mK km s^{-1}. The simulated integrated intensities fall below this 3σ upper limit, at 1.9 mK km s^{-1}.

In the case of CH_2CHCN, a 3σ upper limit to the integrated intensity is calculated to be 2.4 mK km s^{-1} for the $5_{1,5} - 4_{0,4}$ transition of CH_2CHCN. The simulated integrated intensity assuming the same excitation temperature of 5 K was 2.5 mK km s^{-1}, which is just at our detection limit. For the $11_{0,11} - 10_{0,11}$ transition of CH_2CHCN, a 3σ upper limit to the integrated intensity is calculated to be 1.8 mK km s^{-1}. The simulated integrated intensity assuming the same excitation temperature of 5 K was 2.9 mK km s^{-1}, which should have been detected by our observations at the 5σ level. Yet, looking at Fig. 8, we see that there is too much noise to confirm a detection. Also note the detection of this transition was attempted

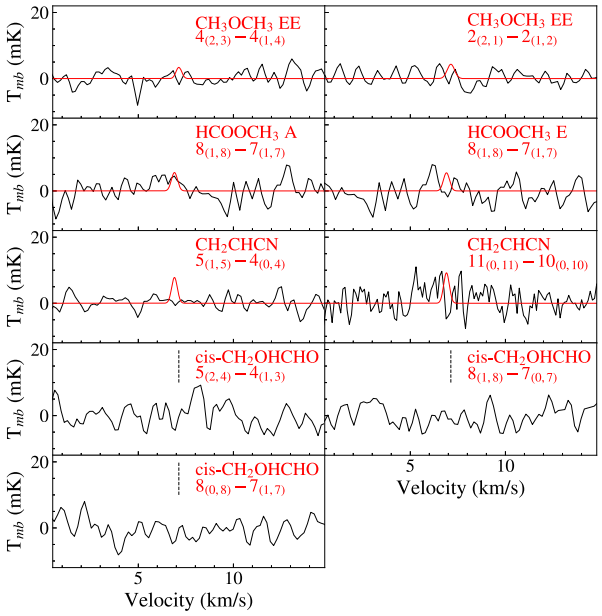

Figure 8. Spectra showing the non-detected transitions as detailed in Table 1. For the non-detected transitions for which we have column density estimates for, their modelled Gaussian LTE spectrum is plotted in red. The attempt to detect the CH_2CHCN $11_{0,11} - 10_{0,11}$ transition done with AROWS backend and therefore has higher velocity resolution, all others were attempted with the MAC backend. For cis-CH_2OHCHO, which was not detected in any transition, a vertical dashed line annotates where we would expect the line to appear, centred on the v_{LSR} of L1521E.

with the new AROWS backend and therefore has higher velocity resolution, all others were attempted with the MAC backend.

3.3.1 *Glycoaldehyde (cis-CH_2OHCHO)*

We attempted to detect three separate transitions of cis-CH_2OHCHO but were unsuccessful. The detection limits are reported in Table 1 and spectra plotted in Fig. 8 (spectroscopic work detailed in Marstokk & Møllendal 1970 and Butler et al. 2001). An especially interesting molecule to target, CH_2OHCHO is one of the simplest sugars (Marstokk & Møllendal 1973), and a constitutional isomer of both acetic acid (CH_3COOH) and the more ubiquitous $HCOOCH_3$. First detected towards Sagittarius B2(N) (Hollis, Lovas & Jewell 2000), as well as towards the high-mass hot core G31.41+0.31 (Beltrán et al. 2009), CH_2OHCHO is likely to form mainly through surface reactions on interstellar dust grains in which HCO is an important constituent (see Butscher et al. 2015; Rivilla et al. 2019; Simons, Lamberts & Cuppen 2020). To date, cis-CH_2OHCHO has not been detected towards a starless core.

3.4 Column density calculations

For CH_3CHO, since the upper energy levels of the five detected A transitions span from 5.0 to 13.9 K, we derive meaningful limits on the excitation temperature and column density. When performing this analysis, we became concerned with source size and filling fraction errors that go into these types of calculations. We include filling fraction as a parameter that goes into the column density measurement as follows

$$N_u = \frac{I}{h A_{ul} f_\nu} \frac{u_\nu(T_{ex})}{[J_\nu(T_{ex}) - J_\nu(T_{cmb})]}, \quad (2)$$

where f_ν is the frequency (or transition) dependent filling fraction, I is the integrated intensity of the line, and u_ν (Planck energy density), and J_ν (Planck function in temperature units) are defined as

$$u_\nu \equiv \frac{8\pi h\nu^3}{c^3} \frac{1}{\exp(h\nu/kT) - 1}, \quad (3)$$

$$J_\nu \equiv \frac{h\nu}{k} \frac{1}{\exp(h\nu/kT) - 1}. \quad (4)$$

In order to get the total column density (N_{tot}) from the upper state value (N_u), the Boltzmann equation in the constant excitation temperature (CTEX) approximation is used

$$\frac{N_u}{g_u} = \frac{N_{tot}}{Q(T_{ex})} \exp(-E_u/kT_{ex}), \quad (5)$$

where $Q(T_{ex})$ is the partition function that depends on excitation temperature, E_u is the upper energy, and g_u the upper state degeneracy. Rotation diagrams are constructed to get estimates for N_{tot} and T_{ex} (right-hand panel of Fig. 9).

Since T_{ex} is still a variable in these equations, an iterative fit is performed where a first guess at T_{ex} is made, and then adjusted depending on the slope of the fit, until both values merge. The partition function, $Q(T_{ex})$, is calculated independently from lists of the rotational energy levels (see section 7 and equation 54 in Mangum & Shirley 2015).

Most calculations in the literature need to assume a filling fraction, f_ν, of 1 since source size is not known a priori. The f_ν parameter is related to both the beam size, which depends on the frequency of the transition observed, and the source size, which, for our purposes, is assumed to be the same for each transition for each oxygen bearing COM molecule. Assuming that the source intensity profile ($I(\theta)$) and the telescope main beam pattern ($P_n(\theta)$) can both be approximated by a Gaussian distribution, then

$$f_\nu = \frac{\int I(\theta) P_n(\theta) d\Omega}{I(\theta = 0) \int P_n(\theta) d\Omega} = \frac{\theta_s^2}{\theta_b^2 + \theta_s^2}, \quad (6)$$

where θ_s is the source FWHM size and θ_b is the 12-m FWHM beam size at the frequency of the transition. In the left-hand panel of Fig. 9, we plot how rotation curve fitted N_{tot} and T_{ex} change with source size for CH_3CHO. For example, at a source size of 57 arcsec (orange line), the purple curve gives the same N_{tot} value as the 'Corrected Source Size' fit in blue in the right-hand panel of Fig. 9. With an average beam size for all five transitions at ∼70 arcsec, if our filling fraction is less than one, i.e. the source size is smaller than 70 arcsec, then N_{tot} will increase strongly with smaller source sizes. The excitation temperature, T_{ex}, in contrast, is nearly independent of source size when beam sizes are kept consistent for one telescope dish diameter.

In order to estimate a source size, we use a CH_3OH map from Nagy et al. (2019) observed with the IRAM 30-m telescope. They do have a CH_3CHO map, however, the lines were not detected with high enough sensitivity (rms ∼ 30 mK) to accurately match emission morphology. We know CH_3OH is one of the simplest and most abundant of the COMs and thus traces the extended COM structure of L1521E. Additionally, CH_3OH and CH_3CHO are thought to be linked chemically (see discussion in Scibelli & Shirley 2020). The area within the FWHM of the peak brightness in the CH_3OH map corresponds to a diameter of 62.9 arcsec (source convolved with the IRAM 30-m beam; $\theta_{src*IRAM}$). When subtracted off in quadrature from the beam size of IRAM at the frequency of CH_3OH (θ_{IRAM} = 25.6 arcsec), source size is found by

$$\theta^2_{src*IRAM} = \theta^2_s + \theta^2_{IRAM}. \quad (7)$$

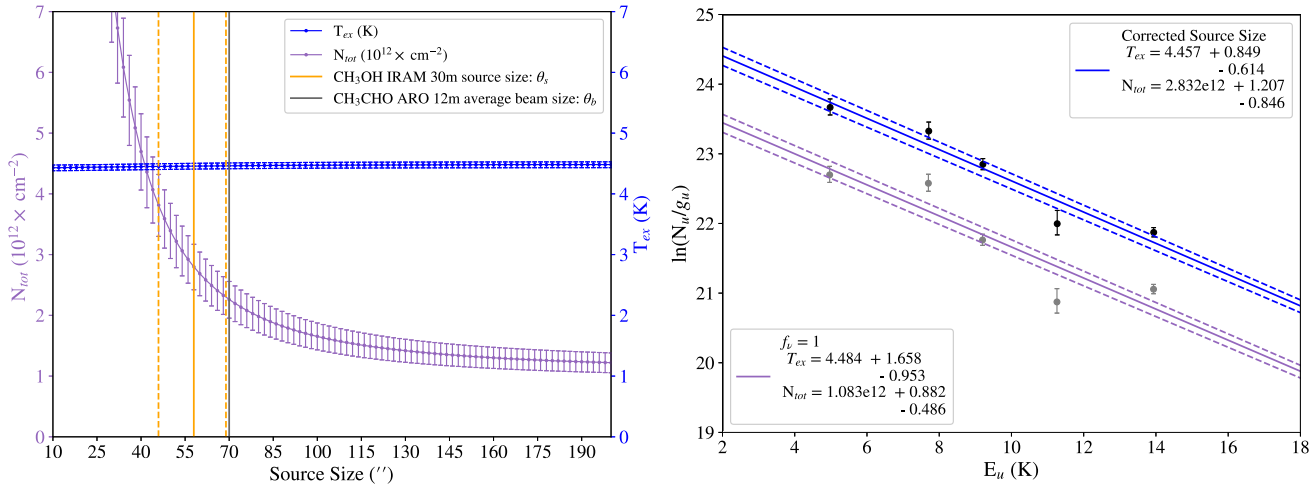

Figure 9. (Left-hand panel) The range of CH_3CHO A column densities as a function of source size is plotted as a purple curve with corresponding values on the left-hand side of the *y*-axis. The shallow sloping blue line represents the range of CH_3CHO A excitation temperature as a function of source size with the corresponding values plotted on the right-hand side of the *y*-axis. The orange line represents the source size calculated from a CH_3OH map of L1521E (Nagy et al. 2019), and dashed lines an uncertainty window of 20 per cent (see Section 3.5). At this source size of 57 arcsec (orange line), the purple curve gives the same N_{tot} value as the 'Corrected Source Size' fit in the right-hand panel. The grey line at 70 arcsec is the average 12-m beam size for all CH_3CHO transitions detected. (Right-hand panel) Rotation diagram for CH_3CHO A showing the difference found if a filling fraction of 1 is assumed (grey points, purple fit) versus if the filling fraction is calculated correctly using the beam and source sizes (black points, blue fit). Instead of errors based on solely the maximum and minimum fit from observed intensity uncertainties (the dashed lines), a least squares analysis is done to find more realistic errors to our linear fit.

Table 3. Column densities and abundances.

Species	CH_3CHO A	CH_3OCH_3 EE	$HCOOCH_3$ E	CH_2CHCN	cis-CH_2OHCHO
Corrected source size					
T_{ex} (K)	$4.46^{+0.85}_{-0.61}$	4.46	4.46	–	–
N_{tot} (10^{12} cm^{-2})	$2.83^{+1.21}_{-0.85}$	$1.59^{+0.27}_{-0.27}$	$4.46^{+1.02}_{-1.02}$	–	–
[a]X wrt. H_2 (10^{-10})	$1.77^{+0.76}_{-0.53}$	$0.99^{+0.17}_{-0.17}$	$2.78^{+0.64}_{-0.64}$	–	–
$f_\nu = 1$					
T_{ex} (K)	$4.48^{+1.66}_{-0.95}$	4.48	4.48	$5.02^{+0.38}_{-0.33}$	4.5
N_{tot} (10^{12} cm^{-2})	$1.08^{+0.88}_{-0.49}$	$0.74^{+0.13}_{-0.13}$	$1.60^{+0.37}_{-0.37}$	$1.00^{+0.37}_{-0.27}$	< 1.84
[a]X wrt. H_2 (10^{-10})	$0.68^{+0.25}_{-0.18}$	$0.46^{+0.08}_{-0.08}$	$1.00^{+0.23}_{-0.23}$	$0.62^{+0.55}_{-0.31}$	< 1.15

Notes. [a]Calculated using the average H_2 column density of $N_{H_2} = 1.6 \times 10^{22}$ cm^{-2}. The excitation temperature, T_{ex}, derived for CH_3CHO is assumed for all other oxygen-bearing species.

The source size is estimated to be $\theta_s = 57$ arcsec (see section 3.5 for uncertainties). When assuming $f_\nu = 1$, N_{tot} is underestimated by a factor of 2.6, compared to when f_ν is corrected given the proper source size (Fig. 9, right-hand panel). Errors in the fit are calculated from a least square fitter. Our range of column densities for CH_3CHO A, reported in Table 3, correcting for source size, is then $N_{tot} = 1.98-4.04 \times 10^{12}$ cm^{-2}. If $f_\nu = 1$ is assumed, we find $N_{tot} = 0.59-1.96 \times 10^{12}$ cm^{-2}. In the right-hand panel of Fig. 9, we also note that for $f_\nu = 1$ there is more scatter away from the linear fit compared to the data points plotted with the corrected source size. Without filling fraction corrections, column densities are underestimated.

For both CH_3OCH_3 and $HCOOCH_3$, the excitation temperatures calculated from our CH_3CHO analysis ($T_{ex} = 4.46$, 4.48 K) are used to derive total column densities. In order to estimate possible uncertainties introduced by this assumption, we calculate column densities given a lower T_{ex} value (at 4.0 K) and a higher T_{ex} value (at 5.5 K), finding a ∼15 per cent increase and decrease, respectively, in column density, which is within our range of error.

In the case of CH_3OCH_3, we only consider the well detected (4σ) EE state transition. Correcting for source size (assuming the same spatial distribution as CH_3OH), a plausible range of column densities are found, $N_{tot} = 1.32-1.86 \times 10^{12}$ cm^{-2}. This corresponds to abundances $X(CH_3OCH_3/H_2) = 0.82-1.16 \times 10^{-10}$ (see Table 3). In the case of $HCOOCH_3$, E state transitions went into the column density analysis, which gives a plausible range $N_{tot} = 3.44-5.48 \times 10^{12}$ cm^{-2}, for corrected source size. This corresponds to an abundance of $X(HCOOCH_3/H_2) = 2.14-3.42 \times 10^{-10}$. In Table 3, column densities are also calculated for CH_3OCH_3 and $HCOOCH_3$ when $f_\nu = 1.0$ is assumed.

Unfortunately, for CH_2CHCN, we are not able make the assumption that CH_3OH traces the same spatial structure in L1521E. Compared to oxygen bearing COMS, we would expect molecules with nitrogen to peak at different locations on the core since molecules such as CO and N_2H^+ are observed to peak differently in starless and pre-stellar cores (e.g. Bacmann et al. 2002, Lippok et al. 2013; see also Jiménez-Serra et al. 2016). As a check, if we assume the same source size as for the oxygen bearing COMs, we find T_{ex}

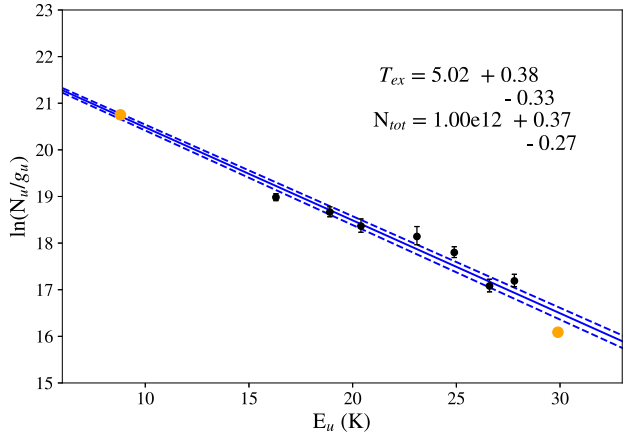

Figure 10. Rotation diagram for CH_2CHCN constructed from seven detected transitions (in black) and two non-detections that we use as 3σ upper limits (in orange). As in Fig. 9, instead of errors based on solely the maximum and minimum fit from observed intensity uncertainties (the dashed lines), a least squares analysis is done to find more realistic errors to our linear fit.

< 5 K, supporting that the assumption is inaccurate. We could have used a simpler nitrogen-bearing COM, such as a CH_3CN map from Nagy et al. (2019), to estimate source size, but this map is too noisy for our purposes (rms ~ 30 mK). The seven transitions of CH_2CHCN that were detected, as well as two upper limit constraints, are used to construct a rotation diagram in the similar manner as done for CH_3CHO, assuming $f_v = 1$ (Fig. 10). The 3σ integrated intensity values for the non-detection's better constrain our fit, due to the extremes in E_u/k at 8.8 and 29.9 K for the 89 and 103 GHz lines, respectively. We find an excitation temperature of $T_{ex} = 5.02^{+0.39}_{-0.33}$ K and range of column densities from $N_{tot} = 0.73-1.37 \times 10^{12}$ cm^{-2}.

3.5 Analysis of uncertainties

We produce χ^2 parameter-space plots for the determination of column density and excitation temperature from CH_3CHO A transitions. By re-arranging equations 2 and 5, we estimate how well the calculated line intensities fit with the observed data for each set of parameters (θ_s, T_{ex}, N) by calculating

$$\chi^2 = \sum_{i=1}^{n} \left(\frac{I_i^{obs} - I_i^{calc}}{\sigma_i^{obs}} \right)^2, \quad (8)$$

where n is the number of transitions observed, which is 5 in our case, I_i^{obs} is the observed integrated intensity, I_i^{calc} is the integrated line intensity predicted by the equations, and σ_i^{obs} is the uncertainty associated with the observed line integrated intensity. In the top panel of Fig. 11, we plot χ^2 as a function of the CH_3CHO A column density and source size (T_{ex} set to 4.46 K); and similarly in the bottom panel χ^2 as a function of the CH_3CHO A column density and T_{ex} (source size set to 57 arcsec). In general, as column density increases, better fits (lower χ^2 values) can be found for small source size and low excitation temperatures. The black dashed lines in Fig. 11 represent the calculated values from our rotation diagram analysis, which cross the minimized portion of the curve where $\chi^2 < 15$. Within this region ($\chi^2 < 15$), excitation temperature is constrained to be between 4.2–5.5 K and N_{tot} between $1.5-3.5 \times 10^{12}$ cm^{-2}, comparable to the uncertainty range from our rotation diagram analysis (blue fit in right-hand panel of Fig. 9). Source size, however, is not as well constrained since it is minimized asymptotically with increasing column densities given source sizes $15 < \theta_s < 74$ arcsec.

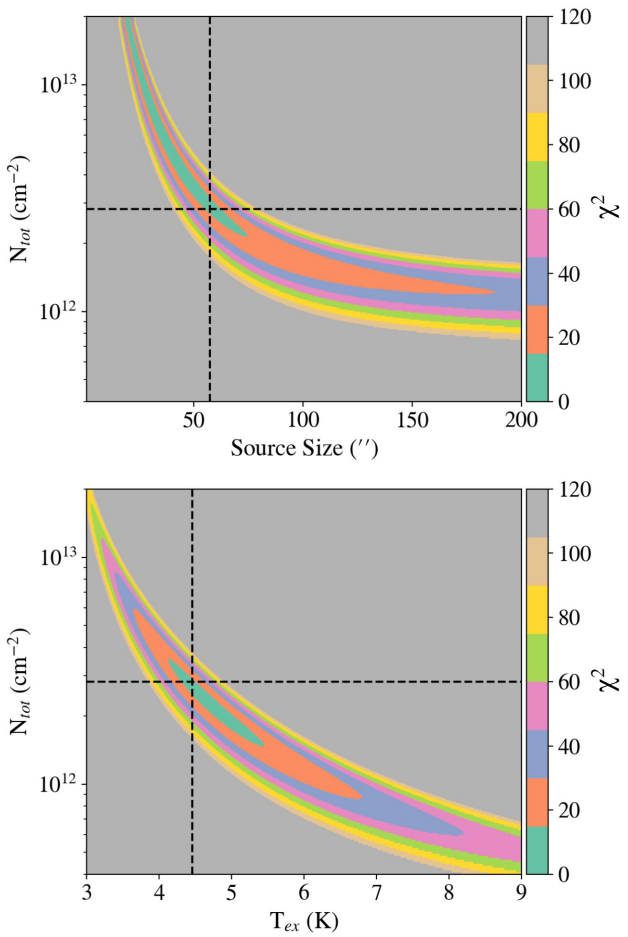

Figure 11. The χ^2-value plots of CH_3CHO A column density versus (top panel) source size ($''$) and (bottom panel) excitation temperature (K). The black dashed lines represent the calculated values found from our rotation diagram analysis, given a source size of 57 arcsec, which crosses the minimized portion of the curve where $\chi^2 < 15$.

Since our χ^2 analysis does not provide a strong constraint on the source size, we must adopt our original assumption that the CH_3OH and CH_3CHO source sizes are the same. In the shocks of L1157, the similar spatial distribution ($\sim$3 arcsec scales) of both species does suggests CH_3OH and CH_3CHO are coming from the same gas (Codella et al. 2020). Similarly, in Nagy et al. (2019) lower ($\sim$30 arcsec) resolution CH_3OH and CH_3CHO maps of L1521E show overlap. If we assume an error of 20 per cent in source size (see left-hand panel of Fig. 9), we find a range of column densities for CH_3CHO, $N_{tot} = 2.3-3.8 \times 10^{12}$ cm^{-2}, which is still within the errors determined from our least squares fit to our rotation diagram (Table 3).

4 DISCUSSION

4.1 Abundance comparison

We compare COM abundances to better understand how L1521E relates to other sites of low-mass star formation (Fig. 12). Since CH_3OH is typically the most abundant COM, we find it interesting to investigate the abundance ratios of COMs w.r.t. CH_3OH, as well w.r.t. H_2. Overall, molecular abundances (w.r.t. H_2) increase between

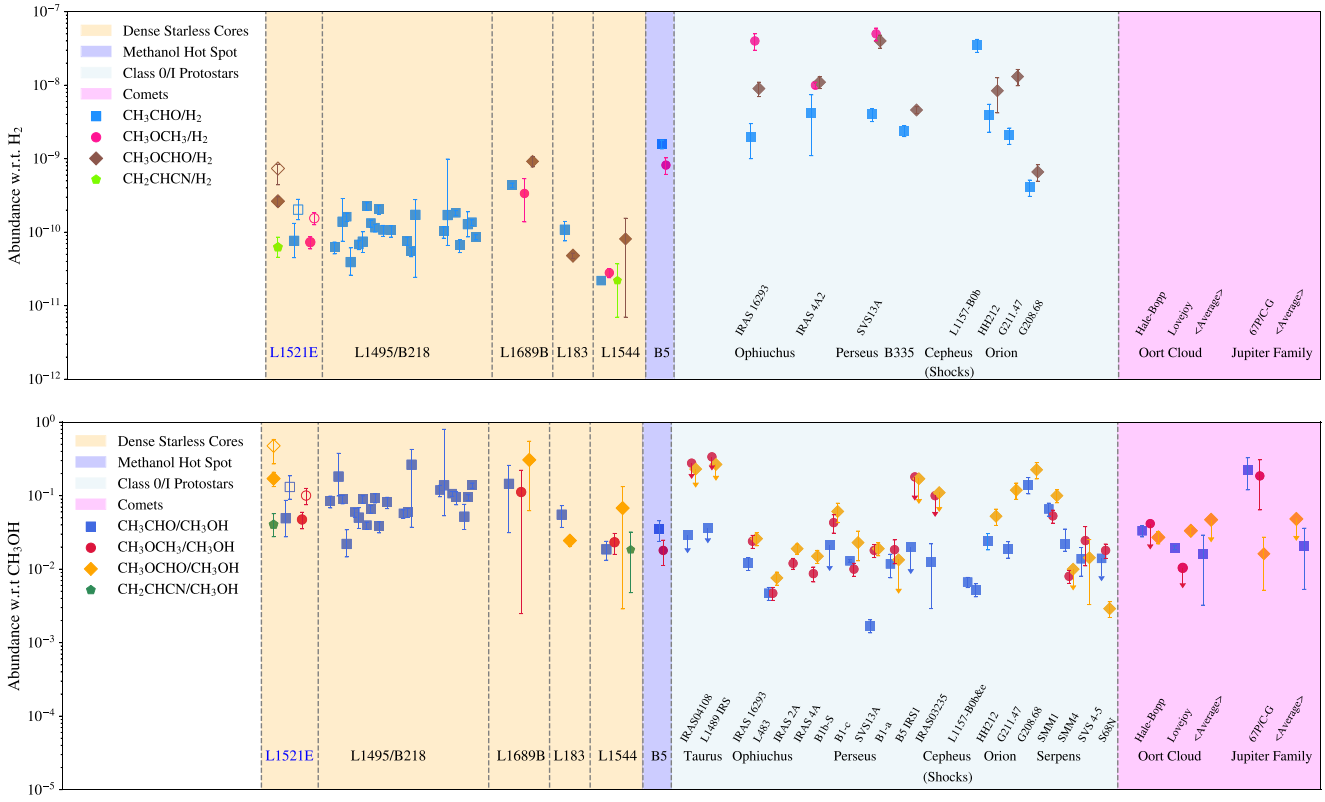

Figure 12. Comparison of COM abundances at various stages of low-mass star formation, including pre-stellar cores, hot cores, and comets. Values for starless cores in L1495/B218 from Scibelli & Shirley 2020, L183 from Lattanzi et al. 2020, L1689B from Bacmann et al. 2012, L1544 from Jiménez-Serra et al. 2016, and for B5 from Taquet et al. 2017. Note that for L1521E, the open symbols represent values where source size was taken into account versus the filled symbols which represent values when $f_\nu = 1$ is assumed. Class 0/I protostars arranged (roughly) by cloud they reside in and/or distance (i.e. L483 has been associated with Serpens in the past but recent *GAIA* data places it at more like 200–250 pc). Protostar references: B1-c, B1-bs, and S68N: ALMA band 3 values from van Gelder et al. 2020; IRAS2A, IRAS4A: Taquet et al. 2015; López-Sepulcre et al. 2017; IRAS 16293-2422: Jaber et al. 2014; Jørgensen et al. 2018; SVS313A: Bianchi et al. 2019; IRAS03245, B1-a, B5 IRS 1, SVS 4-5, IRAS 04108, L1489 IRAS: Graninger, Wilkins & Öberg 2016; Bergner et al. 2017; SMM1, SMM4: Öberg et al. 2011; Taquet et al. 2015; L483: Jacobsen et al. 2019; L1157-B0e & L1157-B0b: Codella et al. 2020; B335: Imai et al. 2016; HH212, G211.47, G208.68: Lee et al. 2019; Hsu et al. 2020. We also include comparisons of the long-range comets, Hale-Bop and Lovejoy (Biver & Bockelée-Morvan 2019), as well as Jupiter-family comet, 67P/Churyumov-Gerasimenko (67/C-G) (Rubin et al. 2019; Schuhmann et al. 2019). Values for 67/C-G are from the mass spectroscopy instrument aboard European Space Agency's Rosetta mission, therefore isomers are indistinguishable (i.e. for CH_3OCHO this includes methyl formate, acetic acid and glycolaldehyde). Upper limit $X(HCOOCH_3/CH_3OH)$ values and range of $X(CH_3CHO/CH_3OH)$ values for all Oort Cloud Comets (OCC) and Jupiter Family Comets (JFC) also from Biver & Bockelée-Morvan (2019).

the pre-stellar and protostellar phase, yet the trend disappears when normalized by methanol.

The total COM abundances summed over all symmetry species are plotted in Fig. 12 for fair comparison with literature values, i.e. in the case for CH_3CHO a total column density of the A + E states is calculated, not just the A state as quoted in Table 3. Two values for each COM abundance value derived for L1521E are also plotted, one if $f_\nu = 1$ was assumed (filled symbols) and one where the source size has been corrected using the assumption of the same spatial distribution as CH_3OH (open symbols).

Ordered roughly in an increasing evolutionary sequence, the molecular abundance w.r.t. H_2 of the starless and pre-stellar cores tends to increase from left- to right-hand, and then drops off after L1689B, in Fig. 12. Most comparable to less-evolved L1521E are the 'typical' starless cores in L1495/B218 as described in Scibelli & Shirley (2020), which range in abundance $X(CH_3CHO/H_2) = 0.4{-}2.2 \times 10^{-10}$. For pre-stellar core L183, embedded in the Serpens cloud, the CH_3CHO abundance falls in between these L1521E/L1495/B218 observations, with $X(CH_3CHO/H_2) = 1.0 \times 10^{-10}$ (Lattanzi et al. 2020).

In the pre-stellar core L1689B, all COM abundances are higher than those found in L1521E, referenced from COM column density values reported in Bacmann et al. (2012) and Bacmann & Faure (2016) assuming a $N(H_2)$ value of 4×10^{22} cm^{-2} (Bacmann et al. 2002). L1689B (central density $>10^6$ cm^{-3}; Steinacker et al. 2016) has been measured to have a relatively low beam-averaged CO depletion factor of $N(H_2)_{S_{850}}/N(H_2)_{C^{17}O} = 2$ at its centre, while for well-studied L1544 the CO beam-averaged depletion factor is >9 at the centre (Lee et al. 2003). L183 in Serpens (central density $> 10^6$ cm^{-3}) sits in the middle of these two cores, as it is more depleted than L1689B but not as much as L1544, with a beam-averaged CO depletion factor $\sim$ 6 (Pagani et al. 2007). Fig. 12 shows that the more highly evolved L1544 (central density $>10^7$ cm^{-3}; Caselli et al. 2019) is deficient in CH_3CHO when compared to all other dense cores at its dust peak position with $X(CH_3CHO/H_2) = 0.22 \times 10^{-10}$. As speculated in Scibelli & Shirley (2020), more evolved cores tend to have lower $X(CH_3CHO/H_2)$ abundances due to the depletion of precursors to COMs and depletion of COMs in the centres of cores.

It could be, however, that environmental effects are causing the large variations between the sources, rather than evolutionary effects.

L1521E, L1495/B218, and L1544 are all located within Taurus and have similar abundance values, i.e. X(CH_3CHO/H_2) varies by at most a factor of 10. As for other COMs, L1544's abundance of CH_3OCH_3 is a factor of ∼3 lower than that of L1521E, with a value of $X(CH_3OCH_3/H_2) = 0.28 \times 10^{-10}$. Abundances of $HCOOCH_3$ and CH_2CHCN are also a factor of ∼3 lower, at $X(HCOOCH_3/H_2) = 0.81 \pm 0.74 \times 10^{-10}$ and $X(CH_2CHCN/H_2) = 0.22 \times 10^{-10}$ (Jiménez-Serra et al. 2016). When we compare the Taurus group (L1521E/L1495/B218/L1544) to L1689B in Ophiuchus, we find, for example, X(CH_3CHO/H_2) is at most 20 times larger. Because L1689B resides in the Ophiuchus molecular cloud, it is subject to different levels of exposure from the interstellar radiation field (ISRF). The radiation field is around two times the standard ISRF for L1689B (Steinacker et al. 2016), whereas for L1544, the strength of the UV field relative to the standard ISRF has only been slightly suppressed ($G_0 = 0.8$; Young et al. 2004). Still, these ISRF intensities (0.8−2.0) towards the dense, obscured cores at high extinction ($A_V > 10$ mag) might not be enough to affect local COM abundances. Differences in dense starless core COM abundances could be due to both their evolutionary stage as well as local environmental conditions. More observations of COMs in dense cores across many clouds are needed to say more.

We place in between the starless core and protostar category the dense cloud B5, which has higher COM abundance (w.r.t. H_2) values out of all the dense cores. Known as a methanol hotspot region, B5 is not classified as pre-stellar or protostellar (Taquet et al. 2017). Every starless and protostellar core plotted in Fig. 12 has a well-defined dust peak in submillimeter continuum emission, yet B5 does not. Thus, we stress that it's position in between starless and protostar does not imply evolution.

The enhancement of COMs in low-mass Classes 0 and I protostars is illustrated in Fig. 12, and is a trend that has been seen before (e.g. López-Sepulcre et al. 2017). In a process laid out recently by Coletta et al. (2020), who observed this same trend in a large sample of massive star-forming regions, molecular abundance will increase through thermal or shock induced desorption of COMs, first formed on ices.

There is also striking similarity (within a few orders of magnitude) between COM abundances w.r.t. CH_3OH, which highlights similar chemical evolution between different stages of low-mass star formation. When comparing abundance values w.r.t. CH_3OH across all evolutionary states, we find that they vary roughly within an order of magnitude. Recent observations show distributions of COM abundances similarly enhanced in the cold component of the low-mass protostars B1-c, S68N, and B1-bs, indicating that COMs could be inherited from the cold pre-stellar core phase (van Gelder et al. 2020). While some COMs could be inherited, the 'warm-up' phase in protostars will increase COM formation efficiency (Garrod & Herbst 2006). Either CH_3OH is more abundant in protostellar sources or less abundant in pre-stellar cores when compared to other COMs (see Section 4.2 for more on formation mechanisms).

Differences in individual protostar COM abundances are due to different physical conditions, since these systems are very dynamic and various heating processes from the accreting protostar, shocks, etc. can affect the local chemical environments. Fig. 12 shows that the L1157B0b shock has the highest X(CH_3CHO/H_2) abundance value (Codella et al. 2020). Additionally, inhomogeneity in analysis techniques can introduce bias when comparing values in the literature.

The recent comet measurements plotted in Fig. 12 (with individual values for Hale-Bopp and Lovejoy) include average ranges for all Oort Cloud Comets (OCC) and as well as all Jupiter Family Comets (JFC) that were reported in tables 1 and 2 in Biver & Bockelée-Morvan (2019). One particular JFC comet, 67P/Churyumov–Gerasimenko (67P/C-G), is plotted separately and has been studied thoroughly by *in situ* measurements from the Rosetta mission (Rubin et al. 2019; Schuhmann et al. 2019). Similarly to protostars, comet abundances w.r.t. CH_3OH are comparable (order of magnitude) as those measured in the plotted cold cores (Fig. 12), suggesting they contain preserved material from pre-Solar system material.

Overall, it is evident that similarities in abundance throughout these stages of low-mass star formation implies that the solid-state processes are already enriching the complex organic inventory during the starless and pre-stellar core phase. Larger sample sets of sources (increased number of cores targeted) as well as COMs (a search for more than a few COMs) are needed to say much more about the link between cold phase and warm phase chemistry.

4.2 Formation mechanisms

Reactive desorption is thought to be one of the important mechanisms needed during the formation of COMs in cold cores. Vasyunin et al. (2017) models COM distribution in well-evolved L1544 with reactive desorption of radicals followed by the rapid gas-phase formation of COMs. The results of their models show that COM species peak in abundance on time-scales of $2 \times 10^4 - 10^5$ yr and at radii of 0.1−0.3 pc, consistent with the position of the CO freeze-out radius in L1544 (see figs 7 and 8 of Vasyunin et al. 2017). At this position, the abundance of the 'surface' CO ice, defined as the top four monolayers in their models, is at its peak.

The density of L1544 at these radii is very near the central density of L1521E at 3×10^5 cm^{-3}. Radiative transfer models of $C^{18}O$ 1-0 and 2-1 are consistent with a factor of a few depletion of CO in the centre of L1521E (Ford & Shirley 2011). So, if CO were depleted by a factor of 2 then 50 per cent of the gas phase CO has already frozen out of the gas phase and formed ice. A small amount of CO freeze-out on to the surface layers can drive radical formation with reactive desorption. In L1521E, the CO depletion radius may essentially be unresolved by current observations and be only in the very central region of the pre-stellar core. It is in these conditions, according to the models of Vasyunin et al. (2017), that the CO surface ice is maximized in abundance and COMs are formed rapidly.

We applied the chemical model described in Vasyunin et al. (2017), with several minor updates described in Nagy et al. (2019), to L1521E, correcting for its more shallower density profile than for L1544. A constant temperature is set to 10 K for our models presented here, and a total gas to dust mass ratio of 150:1 is assumed, to match our dust observations. In this work, we test the 'Minissale&Dulieu' (MD) approach, which changes the reactive desorption efficiency based on ice surface composition as well as on thermodynamics and complexity of products of individual chemical reactions that occur on ice surface (detailed in Minissale et al. 2016). The results obtained with MD model are presented in Fig. 13.

We find that the estimated chemical age of L1521E is indeed young, as COMs first peak $\sim 6.0 \times 10^4$ yr, consistent with the CO depletion age of the core. Our model, however, continues to over estimate CH_3OH abundances by roughly two orders of magnitude, a problem seen before and described in Vasyunin et al. (2017). We find that the observed abundance for CH_3CHO is reproduced by this model within a factor of 2, but the abundances of CH_3OCH_3, $HCOOCH_3$, and CH_2CHCN are underpredicted by factors of 20–160. These COM abundances are underestimated, suggesting that we are either missing a desorption mechanism, or the current description of the already considered mechanisms should be revised in the future.

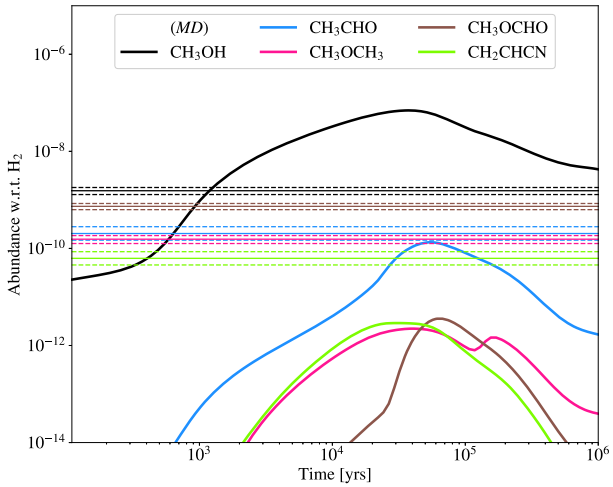

Figure 13. The chemical reactive desorption model used for L1521E is described as the 'Minissale&Dulieu' (MD) approach, where surface reactions dictate desorption efficiency, as described in Minissale et al. (2016) and Vasyunin et al. (2017). Our total (i.e. A + E states for CH_3CHO) calculated abundances, with uncertainties, are plotted as horizontal lines that match the colour scheme of the modelled curves.

The failure of the model to fit CH_3OCH_3 and $HCOOCH_3$ may be partially due to the specific structure of L1521E since it is not as dense as other cores studied, has a low degree of CO freeze-out, and has higher sulfur abundance. Because the density is lower in comparison to L1544, the abundance of H tends to be higher than it is in dense gas. In our model, there is a reaction between atomic H and CH_3O to make CH_3 and OH. With more H, we find CH_3O, which is a precursor of CH_3OCH_3 and, indirectly, $HCOOCH_3$, is destroyed more efficiently leading to lower COM abundances in our model. Additionally, the model is sensitive to the elemental abundance of sulfur, affecting the abundance of atomic hydrogen on the grains through gH + gHS → gH_2S and gH + H_2S → gHS + gH_2 reactions. L1521E has an elevated abundance of S in order to explain observed abundances of S-bearing species in Nagy et al. (2019). The peak abundance of some gas-phase COMs (e.g. CH_3OCH_3) increases when the elemental abundance of S is decreased.

As for CH_2CHCN, it is not reproduced by our model because there are no known efficient routes of its formation in the gas phase (see e.g. KIDA data base; Wakelam et al. 2012). When CH_2CHCN is formed on grains, it does not desorb efficiently to the gas in MD model, because this is a relatively polyatomic species, and energy released during the formation of CH_2CHCN is redistributed between many degrees of freedom in the molecule making the reactive desorption unlikely.

The high COM abundances in the low-density starless core L1521E reveals the importance of alternative formation mechanisms, like non-diffusive chemistry. The non-diffusive chemical models, tailored for L1544, from Jin & Garrod (2020), do show that three-body surface reactions can enhance COMs in the gas phase up to the levels that we see in L1521E as well. In their time-dependent models, CH_3OCH_3 is underproduced while $HCOOCH_3$ is overproduced (see their fig. 2). However, once they optimize the three-body excited-formation efficiency (3-BEF), originally assumed to proceed with 100 per cent efficiency, $HCOOCH_3$ can be matched to the data. Unlike in our chemical reactive desorption models, they do not have the problem of overproducing CH_3OH.

These chemical models have many uncertainties (i.e. extrapolation of reaction rates to 10 K, etc.), and there has not been a complete study of the initial conditions or full parameters space (see Vasyunin et al. 2004, 2008; Wakelam et al. 2005, 2010; Wakelam, Herbst & Selsis 2006). Despite not completely understanding the formation of COMs, we can still propose a basic scenario where the core reaches densities of $\sim 10^5$ cm^{-3} and CO freeze-out rapidly increases, then COMs are formed rapidly assisted by the reactive desorption of radicals and CH_3OH in the ice surface layers. As the central density increases, the COMs also begin to freeze out of the gas phase. The CO depletion radius moves out in the core as does the region of peak COM formation. Thus, peak COM formation proceeds in a wave that moves outwards with time following the CO depletion radius as it propagates through the envelope. When the protostar forms, then the COMs that have frozen out in the densest regions of the core are released from the ices back into the gas phase from the inside outward.

How can we further test which physical mechanism is responsible for the formation of COMs in cold cores? CH_3OCH_3 is an interesting molecule to try and explain in cold environments, due to our current understanding of grain-surface radical chemistry. As demonstrated in Taquet, Wirström & Charnley (2016) and Skouteris et al. (2019), the rate coefficients for the formation process of CH_3OCH_3 by purely gas-phase, ion-molecule routes are not efficient in cold objects like pre-stellar cores. The release of CH_3OCH_3 from the grains to the gas is problematic as laboratory experiments show that it would rather break the molecule (Minissale et al. 2016). One test is to look for the radical precursors that must be present in the gas phase to form the COMs.

Key reactions that are required for the formation of CH_3CHO in our model include the relative slow radiative association of CH_3 + HCO and the neutral–neutral reaction of CH + CH_3OH (Johnson, Blitz & Seakins 2000). HCO and CH_3OH have been detected previously towards L1521E and are abundant ($>10^{-10}$) in the gas phase (Bacmann & Faure 2016; Nagy et al. 2019). CH has its ground state, lambda doubled hyperfine transitions in its lowest energy ladder at 3.3 GHz, but no observations towards L1521E have been published. CH_3 is a planar molecule with no permanent electric dipole moment and cannot be easily observed in cold gas. Recent work has dismissed the formation of CH_3CHO from CH_3OH due to newly computed rate constants, instead favouring a formation route that starts from ethanol and the OH radical (Vazart et al. 2020), further motivating an investigation into alternative COM formation schemes.

An important reaction for the formation of CH_3OCH_3 appears to be the radiative association of CH_3O + CH_3 (i.e. Vasyunin & Herbst 2013; Balucani, Ceccarelli & Taquet 2015). The CH_3O radical was not detected towards L1521E, constraining column density $N < 2.0 \times 10^{11}$ and $X(CH_3O/HCO) < 0.10$ (Bacmann & Faure 2016). For $HCOOCH_3$, which exhibits very similar radial and temporal behaviour as CH_3OCH_3 in the models (Fig. 13), a key chemical species is the hydroxyl radical, OH, which has been shown experimentally to react with CH_3OH to form key radical CH_3O. Our models here, and historically (e.g. Vasyunin & Herbst 2013), have underestimated abundances of $HCOOCH_3$. However, recent studies have shown that $HCOOCH_3$ abundances can be increased by the addition of cosmic ray driven reactions (Shingledecker et al. 2018) and, as previously mentioned, through the non-diffusive surface chemistry (Jin & Garrod 2020).

From comparison of Figs 12 and 13, one can conclude that 'viable' scenarios of formation of COMs in star-forming regions must fulfill two constraints. First, models based on such scenarios must be able to

reproduce observed fractional abundances of COMs w.r.t. hydrogen. Secondly, gas-phase abundance ratios between COMs and CH_3OH must be reproduced. The universality of COMs-to-methanol gas-phase abundance ratios revealed in Fig. 12, supported by the fact that unlike H_2, abundance of CH_3OH can be derived directly in a consistent way with abundances of COMs, suggests very high importance of the second constraint. Our model, as described by Vasyunin et al. (2017), does not fulfill these constraints for L1521E. Thus, the gas-phase scenario of cold COM formation is not sufficient in some cases. These results suggest that COMs observed in cold gas formed not only in gas-phase reactions, but also on surfaces of interstellar grains. Currently, very little is known about exact mechanisms of transport of COMs possibly formed on cold grains ($T \sim 10$ K) to the gas phase.

The detection of a rich COM chemistry in young cold core L1521E presents an interesting challenge for future modelling efforts, requiring some type of unified approach combining cosmic ray chemistry, reactive desorption, and non-diffusive surface reactions.

5 CONCLUSIONS

Observations of COMs in the young starless core, L1521E, sheds light on the initial chemical conditions at one of the earliest stages of star formation. From our molecular line survey, we find the following:

(i) The first detections of CH_3OCH_3, $HCOOCH_3$, and CH_2CHCN in L1521E. Abundance ranges for each of these species are provided; i.e. $X(CH_3OCH_3/H_2) = 0.82-1.16 \times 10^{-10}$, $X(HCOOCH_3/H_2) = 2.14-3.42 \times 10^{-10}$, and $X(CH_2CHCN/H_2) = 0.31-1.17 \times 10^{-10}$.

(ii) A strong constraint on column density and T_{ex} (used to calculate abundances for the other oxygen-bearing COMs) of CH_3CHO from a rotation diagram analysis of five A-state transitions, gives an abundance range $X(CH_3CHO/H_2) = 1.24-2.53 \times 10^{-10}$.

(iii) Without taking into account source size when calculating column densities (i.e. assuming a filling fraction of 1), factors of a few in uncertainty arise. Thus, we stress the importance of high-resolution maps of COMs in upcoming surveys.

(iv) The connection between L1521E, other starless and pre-stellar cores, low-mass hot cores, and comets suggest that some COMs are seeded early on in the star formation process.

(v) The modelled COM formation mechanisms suggest that radical desorption plus gas-phase chemistry alone is not enough to account for the formation of COMs in the cold, dense environments native to pre-stellar cores.

(vi) We suggest that the ratio of gas-phase abundances of COMs to the abundance of methanol is an important constraint for scenarios of formation of complex organic species in star-forming regions.

SOFTWARE

ASTROPY (Astropy Collaboration et al. 2013, 2018), NUMPY (Harris et al. 2020), SCIPY (Virtanen et al. 2020), MATPLOTLIB (Hunter 2007), and GILDAS class (Pety 2005; GILDAS Team 2013)

ACKNOWLEDGEMENTS

We thank our referee, Victor Rivilla, for their insightful comments and for improving the quality of this manuscript. We also thank Paola Caselli, Claudio Codella, Miwha Jin, and Rob Garrod for their valuable conversations and insights that improved this paper. We are thankful that we have the opportunity to conduct astronomical research on Iolkam Du'ag (Kitt Peak) in Arizona and we recognize and acknowledge the very significant cultural role and reverence that these sites have to the Tohono O'odham Nation. We sincerely thank the operators of the Arizona Radio Observatory (Michael Begam, Kevin Bays, Clayton Kyle, and Robert Thompson) for their assistance with the observations. The 12-m telescope is operated by the Arizona Radio Observatory (ARO), Steward Observatory, University of Arizona, with funding from the State of Arizona, NSF MRI Grant AST-1531366 (PI Ziurys), NSF MSIP grant SV5-85009/AST-1440254 (PI Marrone), NSF CAREER grant AST-1653228 (PI Marrone), and a PIRE grant OISE-1743747 (PI Psaltis). Yancy Shirley and Samantha Scibelli were partially supported by NSF Grant AST-1410190 (PI Shirley). Samantha Scibelli is supported by National Science Foundation Graduate Research Fellowship (NSF GRF) Grant DGE-1143953. Anton Vasyunin is supported by the Russian Ministry of Science and Higher Education via the State Assignment Project FEUZ-2020-0038.

DATA AVAILABILITY

The data underlying this article will be shared on reasonable request to the corresponding author.

REFERENCES

Aikawa Y., Wakelam V., Garrod R. T., Herbst E., 2008, ApJ, 674, 984
André P., Di Francesco J., Ward-Thompson D., Inutsuka S. I., Pudritz R. E., Pineda J. E., 2014, in Beuther H., Klessen R. S., Dullemond C. P., Henning T., eds, Protostars and Planets VI, Univ. Arizona Press, Tucson, AZ, p. 27
Astropy Collaboration et al., 2013, A&A, 558, A33
Astropy Collaboration et al., 2018, AJ, 156, 123
Bacmann A., Faure A., 2016, A&A, 587, A130
Bacmann A., Lefloch B., Ceccarelli C., Castets A., Steinacker J., Loinard L., 2002, A&A, 389, L6
Bacmann A., Taquet V., Faure A., Kahane C., Ceccarelli C., 2012, A&A, 541, L12
Balucani N., Ceccarelli C., Taquet V., 2015, MNRAS, 449, L16
Beltrán M. T., Codella C., Viti S., Neri R., Cesaroni R., 2009, ApJ, 690, L93
Benson P. J., Myers P. C., 1989, ApJS, 71, 89
Bergin E. A., Tafalla M., 2007, ARA&A, 45, 339
Bergner J. B., Öberg K. I., Garrod R. T., Graninger D. M., 2017, ApJ, 841, 120
Bertoldi F., McKee C. F., 1992, ApJ, 395, 140
Bianchi E. et al., 2019, MNRAS, 483, 1850
Biver N., Bockelée-Morvan D., 2019, ACS Earth Space Chem., 3, 1550
Butler R. A. H., De Lucia F. C., Petkie D. T., Møllendal H., Horn A., Herbst E., 2001, ApJS, 134, 319
Butscher T., Duvernay F., Theule P., Danger G., Carissan Y., Hagebaum-Reignier D., Chiavassa T., 2015, MNRAS, 453, 1587
Caselli P. et al., 2019, ApJ, 874, 89
Chen H. H.-H. et al., 2019, ApJ, 877, 93
Chuang K. J., Fedoseev G., Qasim D., Ioppolo S., van Dishoeck E. F., Linnartz H., 2017, MNRAS, 467, 2552
Codella C. et al., 2020, A&A, 635, A17
Coletta A., Fontani F., Rivilla V. M., Mininni C., Colzi L., Sánchez-Monge Á., Beltrán M. T., 2020, A&A, 641, A54
Costain C. C., Stoicheff B. P., 1959, J. Chem. Phys., 30, 777
di Francesco J., Evans N. J. I., Caselli P., Myers P. C., Shirley Y., Aikawa Y., Tafalla M., 2007, in Reipurth B., Jewitt D., Keil K., eds, Protostars and Planets V, Univ. Arizona Press, Tucson, AZ, p. 17
Endres C. P., Schlemmer S., Schilke P., Stutzki J., Müller H. S. P., 2016, J. Mol. Spectrosc., 327, 95
Ford A. B., Shirley Y. L., 2011, ApJ, 728, 144
Fuller G. A., Myers P. C., 1992, ApJ, 384, 523
Garrod R. T., Herbst E., 2006, A&A, 457, 927

Gildas Team, 2013, Astrophysics Source Code Library, record ascl:1305.010
Gilmore W., Morris M., Johnson D. R., Lovas F. J., Zuckerman B., Turner B. E., Palmer P., 1976, ApJ, 204, 43
Graninger D. M., Wilkins O. H., Öberg K. I., 2016, ApJ, 819, 140
Harris C. R. et al., 2020, Nature, 585, 357
Herbst E., van Dishoeck E. F., 2009, ARA&A, 47, 427
Hirota T., Ikeda M., Yamamoto S., 2001, ApJ, 547, 814
Hollis J. M., Lovas F. J., Jewell P. R., 2000, ApJ, 540, L107
Hsu S.-Y. et al., 2020, ApJ, 898, 107
Hunter J. D., 2007, Comput. Sci. Eng., 9, 90
Ilyushin V., Kryvda A., Alekseev E., 2009, J. Mol. Spectrosc., 255, 32
Imai M. et al., 2016, ApJ, 830, L37
Jaber A. A., Ceccarelli C., Kahane C., Caux E., 2014, ApJ, 791, 29
Jacobsen S. K., Jørgensen J. K., Di Francesco J., Evans N. J., Choi M., Lee J.-E., 2019, A&A, 629, A29
Jiménez-Serra I. et al., 2016, ApJ, 830, L6
Jiménez-Serra I. et al., 2020, Astrobiology, 20, 1048
Jin M., Garrod R. T., 2020, ApJS, 249, 26
Johnson D. G., Blitz M. A., Seakins P. W., 2000, Phys. Chem. Chem. Phys. (Inc. Faraday Trans.), 2, 2549
Jørgensen J. K., Belloche A., Garrod R. T., 2020, ARA&A, 58, 727
Jørgensen J. K. et al., 2018, A&A, 620, A170
Kirk H., Johnstone D., Tafalla M., 2007, ApJ, 668, 1042
Kirk J. M., Ward-Thompson D., André P., 2005, MNRAS, 360, 1506
Kleiner I., Lovas F. J., Godefroid M., 1996, J. Phys. Chem. Ref. Data, 25, 1113
Lai J. C. Y. et al., 2017, AJ, 154, 206
Lattanzi V., Bizzocchi L., Vasyunin A. I., Harju J., Giuliano B. M., Vastel C., Caselli P., 2020, A&A, 633, A118
Launhardt R. et al., 2013, A&A, 551, A98
Lee C.-F., Codella C., Li Z.-Y., Liu S.-Y., 2019, ApJ, 876, 63
Lee J.-E., Evans N. J. I., Shirley Y. L., Tatematsu K., 2003, ApJ, 583, 789
Lippok N. et al., 2013, A&A, 560, A41
López-Sepulcre A. et al., 2017, A&A, 606, A121
Makiwa G., Naylor D. A., van der Wiel M. H. D., Ward-Thompson D., Kirk J. M., Eyres S., Abergel A., Köhler M., 2016, MNRAS, 458, 2150
Mangum J. G., Shirley Y. L., 2015, PASP, 127, 266
Marstokk K. M., Møllendal H., 1970, J. Mol. Struct., 5, 205
Marstokk K. M., Møllendal H., 1973, J. Mol. Struct., 16, 259
Minissale M., Dulieu F., Cazaux S., Hocuk S., 2016, A&A, 585, A24
Müller H. S. P., Schlöder F., Stutzki J., Winnewisser G., 2005, J. Mol. Struct., 742, 215
Müller H. S. P., Thorwirth S., Roth D. A., Winnewisser G., 2001, A&A, 370, L49
Nagy Z., Spezzano S., Caselli P., Vasyunin A., Tafalla M., Bizzocchi L., Prudenzano D., Redaelli E., 2019, A&A, 630, A136
Neustock W., Guarnieri A., Demaison J., Wlodarczak G., 1990, Z. Nat.forsch. A, 45, 702
Öberg K. I., Bottinelli S., Jørgensen J. K., van Dishoeck E. F., 2010, ApJ, 716, 825
Öberg K. I., van der Marel N., Kristensen L. E., van Dishoeck E. F., 2011, ApJ, 740, 14
Ossenkopf V., Henning T., 1994, A&A, 291, 943
Pagani L., Bacmann A., Cabrit S., Vastel C., 2007, A&A, 467, 179
Pattle K. et al., 2015, MNRAS, 450, 1094
Pety J., 2005, in Casoli F., Contini T., Hameury J. M., Pagani L., eds, SF2A-2005: Semaine de l'Astrophysique Francaise, EdP-Sciences, Strasbourg, p. 721
Pickett H. M., Poynter R. L., Cohen E. A., Delitsky M. L., Pearson J. C., Müller H. S. P., 1998, J. Quant. Spec. Radiat. Transf., 60, 883
Redman M. P., Rawlings J. M. C., Nutter D. J., Ward-Thompson D., Williams D. A., 2002, MNRAS, 337, L17
Rivilla V. M., Beltrán M. T., Vasyunin A., Caselli P., Viti S., Fontani F., Cesaroni R., 2019, MNRAS, 483, 806
Rubin M. et al., 2019, AGU Fall Meeting Abstracts, #P43C
Schuhmann M. et al., 2019, ACS Earth and Space Chem., 3, 1854
Scibelli S., Shirley Y., 2020, ApJ, 891, 73
Seo Y. M. et al., 2015, ApJ, 805, 185
Seo Y. M. et al., 2019, ApJ, 871, 134
Shingledecker C. N., Tennis J., Le Gal R., Herbst E., 2018, ApJ, 861, 20
Shirley Y. L., Nordhaus M. K., Grcevich J. M., Evans N. J. I., Rawlings J. M. C., Tatematsu K., 2005, ApJ, 632, 982
Simons M. A. J., Lamberts T., Cuppen H. M., 2020, A&A, 634, A52
Sipilä O., Harju J., Juvela M., 2011, A&A, 535, A49
Skouteris D., Balucani N., Ceccarelli C., Faginas Lago N., Codella C., Falcinelli S., Rosi M., 2019, MNRAS, 482, 3567
Standards U. S. N. B. O., Wacker P., 1969, Microwave Spectral Tables: Polyatomic Molecules with Internal Rotation, Univ. Michigan, Ann Arnor, MI
Steinacker J., Bacmann A., Henning T., Heigl S., 2016, A&A, 593, A6
Suzuki H., Yamamoto S., Ohishi M., Kaifu N., Ishikawa S.-I., Hirahara Y., Takano S., 1992, ApJ, 392, 551
Tafalla M., Santiago J., 2004, A&A, 414, L53
Taquet V., López-Sepulcre A., Ceccarelli C., Neri R., Kahane C., Charnley S. B., 2015, ApJ, 804, 81
Taquet V., Wirström E. S., Charnley S. B., 2016, ApJ, 821, 46
Taquet V., Wirström E. S., Charnley S. B., Faure A., López-Sepulcre A., Persson C. M., 2017, A&A, 607, A20
van Gelder M. L. et al., 2020, A&A, 639, A87
Vastel C., Ceccarelli C., Lefloch B., Bachiller R., 2014, ApJ, 795, L2
Vasyunin A. I., Caselli P., Dulieu F., Jiménez-Serra I., 2017, ApJ, 842, 33
Vasyunin A. I., Herbst E., 2013, ApJ, 769, 34
Vasyunin A. I., Semenov D., Henning T., Wakelam V., Herbst E., Sobolev A. M., 2008, ApJ, 672, 629
Vasyunin A. I., Sobolev A. M., Wiebe D. S., Semenov D. A., 2004, Astron. Lett., 30, 566
Vazart F., Ceccarelli C., Balucani N., Bianchi E., Skouteris D., 2020, MNRAS, 499, 5547
Virtanen P. et al., 2020, Nature Methods, 17, 261
Wakelam V., Herbst E., Le Bourlot J., Hersant F., Selsis F., Guilloteau S., 2010, A&A, 517, A21
Wakelam V., Herbst E., Selsis F., 2006, A&A, 451, 551
Wakelam V., Selsis F., Herbst E., Caselli P., 2005, A&A, 444, 883
Wakelam V. et al., 2012, ApJS, 199, 21
Watanabe N., Kouchi A., 2002, ApJ, 571, L173
Young K. E., Lee J.-E., Evans N. J. I., Goldsmith P. F., Doty S. D., 2004, ApJ, 614, 252

This paper has been typeset from a TEX/LATEX file prepared by the author.